Mobility of solid and porous hollow SiO2 nanoparticles in saturated porous media: Impacts of surface and particle structure

Mobility of Solid and Porous Hollow SiO_2 Nanoparticles in Saturated Porous Media: Impacts of Surface and Particle Structure

Vinicius Bueno[1], Alessandro Bosi[2], Tiziana Tosco[2] and

Subhasis Ghoshal[1,*]

[1] *Department of Civil Engineering, McGill University, Montreal, Quebec H3A 0C3, Canada*

[2] *Department of Environment, Land and Infrastructure Engineering (DIATI), Politecnico di Torino, C.so Duca degli Abruzzi 24, 10129 Torino, Italy*

Published in Journal of Colloid and Interface Science

Link to Publisher's page:

https://doi.org/10.1016/j.jcis.2021.07.142

*Corresponding author, e-mail: subhasis.ghoshal@mcgill.ca, Phone: (1)-514-398-6867; Fax: (1)-514-398-7361

Graphical Abstract:

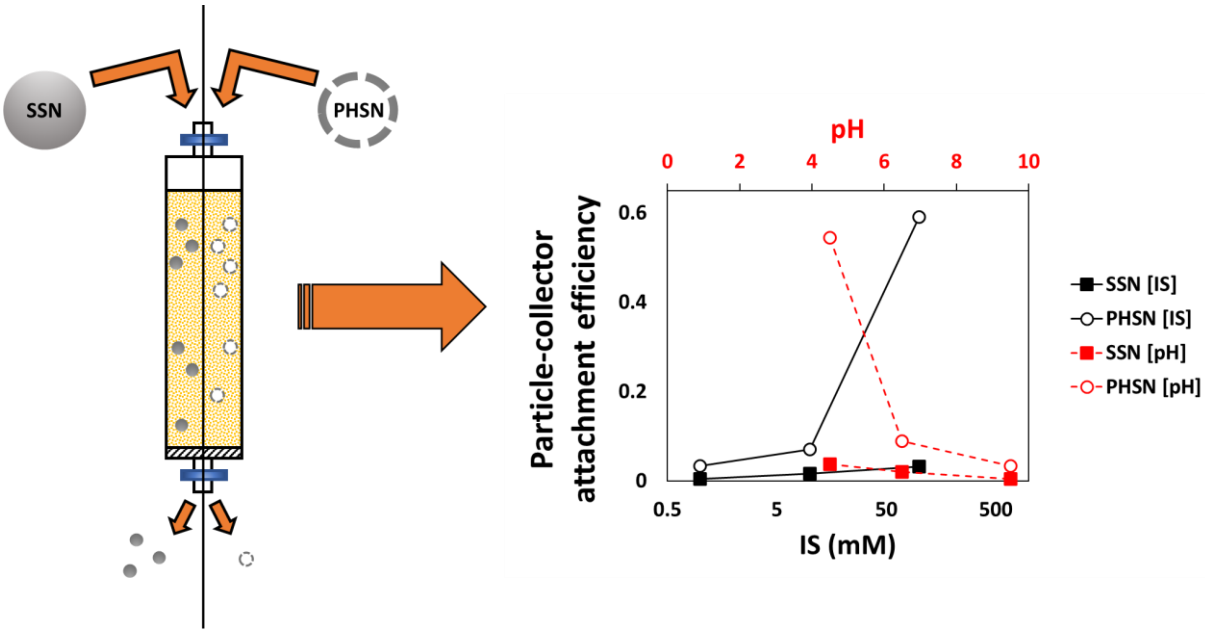

HIGHLIGHTS:

- The porous shell in porous hollow silica nanoparticles (PHSN) resulted in significantly different particle physicochemical properties compared to solid silica nanoparticles (SSN) of similar size.
- Higher surface roughness in PHSN than that of SSN was responsible for the deviations in standard DLVO theory.
- High ionic strength (IS) and low pH decreased mobility and increased retention for both particle populations.
- Retention was 3-fold higher for PHSN compared to SSN at the highest IS and lowest pH.

ABSTRACT

Silica nanoparticles (SiO_2 NPs) are of increasing interest in nano-enabled agriculture, particularly as nanocarriers for the targeted delivery of agrochemicals. The direct application of these in agricultural soils may lead to the release of SiO_2 NPs in the environment. Although some studies have investigated transport of solid SiO_2 NPs in porous media, there is a knowledge gap on how different SiO_2 NP structures incorporating significant porosities can affect the mobility of such particles under different conditions. Herein, we investigated the effect of pH and ionic strength (IS) on the transport of two distinct structures of SiO_2 NPs, namely solid SiO_2 NPs (SSNs) and porous hollow SiO_2 NPs (PHSN), of comparable sizes (~200 nm). Decreasing pH and increasing ionic strength reduced the mobility of PHSNs in sand-packed columns more significantly than for SSNs. The deposition of PHSNs was approximately 3 times greater than that of SSNs when pH was 4.5 and IS 100 mM. The results are non-intuitive given that PHSN has a lower density and the same chemical composition of SSN but can be explained by the greater surface roughness and ten-fold greater specific surface area of PHSN, and their impacts on van der Waals and electrostatic interaction energies.

Introduction

Rapid advances in nano-enabled agriculture have been focused on making significant improvements in enhancing crop yields, mitigating energy and water footprints, and reducing unintended pollution from the use of fertilizers and pesticides [1-3]. The latter is achieved through precise delivery of pesticides and fertilizers using nanocarriers, which can dose these agents to plant tissues in a targeted manner and with a higher efficiency than traditional pesticide and fertilizer formulations [3-8]. Porous nanosilica is a promising candidate for pesticide and fertilizer nanocarriers because SiO_2 is an earth-abundant, biocompatible material [9, 10] that promotes plant growth, and provides resistance towards pathogens and unfavorable environmental conditions [10-12]. SiO_2 nanocarriers may be introduced to agricultural soils either through direct application or through indirect releases such as discharges to soils following foliar application [13-17]. It is important to investigate the mobility of silica nanocarriers to account for their environmental transport and that of their cargo. Although several studies have investigated the transport of SSNs in geologic deposits [18-21], it is unclear how the differences in particle structure, in particular the high porosity of silica nanocarriers, fundamentally influence their mobility in porous media.

Among studies on SSN transport, Wang, et al. [20] reported that particle size and concentration influenced the transport and retention profiles of SSN in porous media. Small SSN of 8 nm diameter caused higher retention and, thus, less mobility when compared to SSN with mean diameter of 52 nm. Moreover, that study showed that increased ionic strength reduced the overall SSN mobility in the porous medium. Zhang, et al. [22] reported that humic acid improved mobility of SiO_2 nanoparticles in saturated porous media because of enhanced electrostatic forces. HonetschlÄgerová, et al. [23] showed that coating nanoscale zerovalent iron (nZVI) particles with a SiO_2 shell enhanced their colloidal stability and mobility in porous media compared to bare nZVI, which have high aggregation tendency and thus are very colloidally unstable.

Common parameters that influence the mobility of nano- and micro-colloids in porous media are (i) particle surface charge and coating [23], (ii) particle size [20], (iii) ionic strength [24], (iv) pH [25], and (v) temperature [26]. However, few studies have analyzed the effects of the structure of nanoparticles. For SiO_2 nanoparticles, while most studies investigate the

transport of SSNs, most applications in agriculture focus on the use of mesoporous SiO_2, such as MCM-41 [27-31], and SiO_2 nanoshells, such as PHSN [32-36], which are structurally different from SSNs and, therefore, may lead to different transport profiles. Given the increasing use of silica nanocarriers in agriculture, and the increased potential for release into soils, there is a critical knowledge gap on the transport behavior of nanocarriers in natural porous media, and whether their transport differ from those of SSN which have been studied before.

The objective of this study was to evaluate how the porous structure of the SiO_2 NPs influences their mobility. Two SiO_2 NPs with very distinct structure and similar size were synthesized, namely (i) SSNs which are solid spheres and (ii) PHSNs which are porous and hollow and represent nanocarriers with high porosity. The synthesis methods ensured that the particles were composed only of SiO_2. Experiments were conducted to assess the colloidal stability and mobility of these two particles in saturated, acid-washed, sand-packed columns, over a range of pH and ionic strength (IS). Furthermore, theoretical Derjaguin-Landau-Verwey-Overbeek (DLVO) interaction energies and single collector contact efficiency calculations were performed to investigate how porosity and density differences in the two types of particles influenced colloidal stability and deposition on collector surfaces. A fundamental understanding of the impacts of particle structure on its mobility is essential before investigation of the effects of various environmental conditions and complex particle compositions.

Materials and Methods

Porous Media. White quartz sand with 50-70 mesh particle size (Sigma-Aldrich) was used as the porous medium in this study. Scanning electron microscopy was used to confirm the sand grain morphology and size (Figure S1). The average grain diameter of the quartz sand was 250 μm, with diameters ranging from 210 to 297 μm. Prior to use, the sand was treated with HNO_3 (70% v/v) for 16 hours to remove metal oxides and other impurities as reported elsewhere [37-40]. The acid-washed sand was thoroughly rinsed with DI water (ASTM Type 1, Thermo Fisher) followed by three 20-minute cycles of sonication in water bath. The cloudy

DI water was replaced at the end of each cycle. The electrical potential on the surface of the sand particles was quantified by measuring the zeta potential under varying conditions of pH and IS, remaining negatively charged across the board (Table S1).

SiO_2 Nanoparticles. SSNs were synthesized following a protocol based on the Stöber method [41]. A solution of anhydrous ethanol (200 mL, 100%, Commercial Alcohols, Canada) and NH_4OH (15 mL, 28% NH_3 basis, Sigma-Aldrich) was stirred under 400 rpm for 30 minutes to ensure complete mixing. Then, 10 mL of tetraethyl orthosilicate (TEOS 98%, Sigma-Aldrich) was added dropwise at a rate of 1 mL/min. After 5 hours, the reaction was stopped by drying the cloudy suspension overnight at 80^{o}C. Finally, the nanoparticles were calcined for 5h under 500^{o}C.

PHSNs were synthesized based on a protocol previously described [36]. In summary, a solution of DI water (125 mL), anhydrous ethanol (75 mL), NH_4OH (7.5 mL), hexadecyltrimethylammonium bromide (CTAB, 300 mg, Sigma-Aldrich) and Pluronic P123 (850 mg, Sigma-Aldrich) was stirred under 1000 rpm for 1 hour until reagents were completely mixed. Then, 10 mL of TEOS was added dropwise at a rate of 0.75 mL/min. After 5 hours, the reaction was stopped by drying the cloudy suspension overnight at 80^{o}C. Finally, the nanoparticles were calcined for 5h under 500^{o}C.

The morphology of the nanoparticles was characterized by TEM using a Philips model CM200 TEM at an acceleration voltage of 200 kV. The particle size distribution was characterized through DLS using Malvern Zetasizer Nano ZS (Malvern Instruments, UK). DLS analysis was conducted using SSN and PHSN suspended in DI water with a concentration of 100 ppm. The specific surface area was determined using the BET method through nitrogen sorption/desorption experiments using a Quantachrome Autosorb-1 (Quantachrome GmbH & Co., Netherlands). FTIR spectra were obtained for both SSN and PHSN with a Spectrum II (Perkin Elmer) Spectrometer with a single bounce diamond crystal. Spectra were recorded in the range from 4000 to 400 cm^{-1} at a resolution of 1 cm^{-1}.

Solution Chemistry. 100 ppm of SSNs and PHSNs were prepared by suspending the dried SiO_2 powder obtained from the synthesis in DI water, followed by sonication in water bath for 30 minutes. IS was adjusted in the nanoparticle suspensions and background solutions

using NaCl (ACS grade, Sigma-Aldrich). The pH was adjusted dropwise with 0.1 M HCl and 0.1 M NaOH, and the counter-ions (Na^+ and Cl^-) were taken into account for the final IS of the system.

Column Experiments. A 10-cm long acrylic column (Chromaflex, Fisher) with internal diameter of 1 cm was packed with acid-washed sand using a wet packing technique described in Oliviera, et al. [42]. Prior to the addition of the acid-washed sand, the column was filled with DI water. Then, saturated acid-washed sand was deposited in increments of 1 cm layer at a time while vibrating the column for 20 seconds. This procedure was repeated until the saturated acid-washed sand occupied the whole space within the 10 cm long column, yielding a porosity of 0.391 from fitting the advection dispersion equation to the tracer breakthrough curve (BTC).

At the start of each run, 3 pore volumes (PVs) of DI water were introduced to the system with the aid of a peristaltic pump at a flow rate of 1.25 mL/min, which corresponds to a Darcy velocity of 2.64×10^{-4} m s^{-1} within our setting. The flow rate remained constant throughout the run and for all the different conditions. 10 PVs of background solution amended with NaCl (25 mM) followed to produce the breakthrough curve (BTC) for the tracer to ensure consistency and reproducibility of the column wet packing procedure. Then, 5 PVs of particle-free electrolyte solution at desired IS and pH, 10 PVs of the particle suspension at 100 ppm at the respective IS and pH. Then 5 PVs of the particle-free electrolyte solution and, finally, 3 PVs of DI water were injected. Ten different experimental conditions were carried out in triplicates as detailed in Table 1. The SiO_2 NP concentration of 100 ppm was selected based on concentrations employed in previous column transport studies for SSN [20] and concentrations relevant to foliar application of SiO_2 NPs [13].

NaCl and particle (SSN and PHSN) concentrations exiting the column were quantified in real-time by UV-Vis spectroscopy (Agilent Technologies, Model 8453) in a quartz flow-through cell (Hellma Analytics, GE, 10 mm path length, 300 μL volume) at wavelengths of 196 nm, and 350 nm, respectively. Particle size distribution and zeta potential at different experimental conditions were measured using a Zetasizer Nano ZS (Malvern Instruments). Size distribution was determined using the dynamic light scattering (DLS) mode and electrophoretic mobility mode [43].

Table 1. Particle characterization data and calculated DLVO interaction energies by nanoparticle type, pH, IS (mM, electrolyte NaCl), and measurements of zeta potential (mV), Z-average diameter (nm), Polydispersity Index (PdI), depths of primary minima (Φ_{min}), heights of energy barriers (Φ_{max}) and depths of secondary wells (Φ_{sec}) for the DLVO energy profiles. Errors denote standard deviations corresponding to measurement of 3 samples.

Experiment	Structure	pH	IS (mM)	Zeta Potential (mV)	Z-avg dia. (nm)	PdI	Particle-Particle (k_bT)			Particle-Collector (k_bT)		
							Φ_{min}	Φ_{max}	Φ_{sec}	Φ_{min}	Φ_{max}	Φ_{sec}
Exp 1	SSN	4.5	1	-34.6 ± 0.9	238 ± 1.9	0.14 + 0.01	-160.4	120.2	/	-789.2	178.7	/
Exp 2	SSN	6.5	1	-52.5 ± 0.8	229 ± 5.4	0.12 ± 0.02	-4.5	255.7	/	-555.9	355.4	/
Exp 3	SSN	9.5	1	-71.3 ± 1.3	201 ± 4.9	0.05 ± 0.02	152.4	373.2	/	-289.6	495.5	/
Exp 4	SSN	9.5	10	-57.3 ± 1.1	214 ± 4.8	0.07 ± 0.03	33.2	238.0	/	-381.7	358.5	/
Exp 5	SSN	9.5	100	-37.4 ± 3.0	220 ± 3.6	0.07 ± 0.02	-132.5	82.8	-0.6	-587.9	171.2	-2.0
Exp 6	PHSN	4.5	1	-10.7 ± 0.7	240 ± 1.1	0.20 ± 0.02	-142.0	10	/	-791.3	49.1	/
Exp 7	PHSN	6.5	1	-29.2 ± 1.1	239 ± 1.8	0.19 ± 0.02	-52.6	90.4	/	-601.3	210.9	/
Exp 8	PHSN	9.5	1	-42.5 ± 2.0	221 ± 1.9	0.20 ± 0.01	47.0	173.8	/	-387.0	349.3	/
Exp 9	PHSN	9.5	10	-42.1 ± 1.5	220 ± 3.1	0.27 ± 0.03	42.3	155.8	/	-391.6	296.7	/
Exp 10	PHSN	9.5	100	-31.3 ± 0.5	239 ± 2.0	0.18 ± 0.02	-41.6	72.3	-0.3	-536.6	158.2	-1.9

Interaction Energies and Collector Efficiency. The van der Waals forces and repulsive electrostatics forces for SSN and PHSN for the different experimental conditions were calculated to determine the particle-particle and particle-collector interaction energies according to the classical DLVO model (Equation 1) using the expressions proposed by Gregory [44] (full list of equations and theoretical considerations in Supporting Information). Interaction energies due to Born were not accounted for because of their negligible magnitudes [45-47]. The Hamaker constant was calculated using the expressions proposed by Lipkin, et al. [48], and accounted for the contributions of water core and silica shell for PHSNs The full list of physical properties used to compute the DLVO energy profiles for SSNs and PHSNs can be found in Table S2. For PHSNs, the interior and exterior fluid compositions were considered to be the same, thus the van der Waals energy profile was calculated by subtracting the resulting forces generated by a particle with diameter corresponding to the inner diameter of the PHSN from the resulting forces calculated for a particle with diameter corresponding to the outer diameter of the PHSN [49, 50] as per Equation 2.

$$V_{tot} = V_{vdW} + V_{edl} \quad (1)$$

$$V_{vdW} = V_{vdW}^{out} - V_{vdW}^{in} \quad (2)$$

The depths of primary minima (Φ_{min}), heights of energy barriers (Φ_{max}) and depths of secondary wells (Φ_{sec}) for the DLVO energy profiles are summarized in Table 1.

The single collector contact efficiency was calculated based on the empirical expressions derived from the following studies: Yao, et al. [51], Rajagopalan and Tien [52], Tufenkji and Elimelech [53], Ma, et al. [54], Nelson and Ginn [55], Ma, et al. [56], and Messina and Sethi [57]. The comprehensive list of expressions used in this step is presented in Table S3.

Results and Discussion

SiO_2 NPs Characterization. The TEM images in Figure 1 show that while the SSN synthesized based on the Stöber method (Figure 1a and b) are solid with an average primary particle diameter of 184 nm, the PHSN (Figure 1c and d) are hollow with an average diameter of 205 nm. Figure 1b and 1d show a more magnified TEM image of singular particles of SSN and PHSN. The shell thickness of the PHSN ranged from 22 to 38 nm. An important difference in the surface characteristics of the two particle types is the significantly higher surface roughness of PHSN created in part by the highly porous shell surface. The calculated mass of the SSNs and PHSNs were very similar. Thus, the particle number concentration of SSNs and PHSNs were very similar in all experiments.

The primary particle size distributions (N = 100) for SSN and PHSN represented in Figure S2a and Figure S2b, respectively, show that both particles have a comparable size distribution. The hydrodynamic diameter size distribution, obtained by DLS for SSNs (Figure 2a) is slightly narrower than for PHSNs (Figure 2b) as reported in Table 1 represented by the polydispersity index (PdI). The DLS measurements were obtained at pH 9.5 and IS 1 mM because optimal colloidal stability was obtained at these conditions. Overall, both particle populations were successfully synthesized to yield comparable size and shape, to enable direct comparison of their mobility in porous media.

The surface characteristics were investigated using BET and FTIR analyses (Figure S3). Although, SSN and PHSN have relatively similar sizes, the specific surface area of PHSN (287 ± 30 m^2 g^{-1}) is approximately 10 times greater than the specific surface area of SSN (29 ± 8 m^2 g^{-1}). This is due to the presence of micro-scale pores of around 2.5 nm in the PHSN surface as characterized in previous work [36].

The chemical composition of the SSN and PHSN were identical with no chemical bonds present other than those attributable to silica, as determined by FTIR analyses (Figure S3c). Although both populations of SiO_2 nanoparticles have the same chemical composition, the differences in their structure result in different Hamaker constants (6.59×10^{-21} J for SSNs and 5.79×10^{-21} J for PHSNs) and zeta potentials (Table 1). Given the higher surface area of

PHSN, there are more counter-ions around the PHSNs compared to SSNs, resulting in a thinner solvation layer and zeta potential closer to zero [58].

pH Effect of the Transport Behavior. The effect of pH in the transport of SSNs and PHSNs in saturated porous media was evaluated at IS 1 mM for both sets of nanoparticles. The BTCs obtained for SSNs (Figure 3a) show that the values for steady-state relative effluent concentration (at 9 PV) decreased as the pH also decreased, from 0.99 at pH 9.5, to 0.95 at pH 6.5 and then 0.91 at pH 4.5, suggesting that transport of SSNs is slightly hindered as the pH becomes more acidic, increasing retention of SSNs in the column. The changes in mobility of SSNs with pH are consistent with another study showing reduced mobility of SiO_2 nanoparticles in carbonate reservoirs at acidic pH [59]. It should be noted that the SSN hydrodynamic diameter as measured by DLS increased slightly with pH decrease from 9.5 to 4.5 (from 201 ± 4.9 nm at pH 9.5 to 238 ± 1.9 nm at pH 4.5) suggesting limited aggregation.

The DLVO energy profiles for the SSN particle-particle (Figure 4a) and particle-collector interactions (Figure 4c) at IS of 1 mM, show highly unfavorable attachment conditions. Under these conditions, the repulsion forces between SSNs and between SSNs and the sand collector surfaces resulted in elevated energy barriers and absence of secondary minima (Table 1). The DLVO energy profiles for the SSN particle-collector interactions (Figure 4c) support the observations of low retention of SSNs from the BTC trends discussed above (Figure 3a). The calculated particle-particle energy barrier for SSN at pH 4.5 was far greater than 15 k_bT, an approximate threshold for colloidal stability, and thus do not suggest conditions favorable for SSN aggregation. However, the energy barrier was significantly lower at pH 4.5 (120.2 k_bT) compared to pH 9.5 (373.2 k_bT).

The values for steady-state relative effluent concentrations in the BTCs for PHSN also decreased with decreasing pH, from 0.94 at pH 9.5 to 0.85 at pH 6.5 and then more substantially to 0.37 at pH 4.5. The extent to which the transport was hindered in PHSNs with decreasing pH was much more significant than that in SSNs. As with SSNs, there was also a small increase in DLS-measured hydrodynamic diameters with decreasing pH (221 ± 1.9 nm at pH 9.5 to 240 ± 1.1 at pH 4.5). Although the DLVO calculations suggest that the primary maximum for particle-particle interactions of PHSN at pH 4.5 was small at 10 k_bT, the measured hydrodynamic diameters suggest limited aggregation, comparable to SSNs.

At pH 4.5 and IS 1of mM, the primary energy maximum for PHSN was the lowest (49.1 k_bT) of the 3 pH conditions at the same IS, and thus the DLVO calculations are in qualitative agreement with the experimental observation of significantly low mobility of PHSNs at pH 4.5. However, there was no secondary minima predicted by DLVO calculations. This suggests that other parameters played a role in the transport of these nanoparticles. Straining is unlikely to be a cause for the significantly higher deposition of PHSN, given that the SSN have similar hydrodynamic diameters at corresponding pH, but had lower deposition. Furthermore, straining is not expected when the colloid diameter (d_c) to sand grain diameter (d_g) ratio (d_c/d_g) is below 0.008 [60]. Here, the d_p/d_g ratio is approximately 0.001 for both SSN and PHSN. According to Xu, et al. [60], straining rates are negligibly small when d_p/d_g < 0.008 and, in this work, such ratio is one order of magnitude lower. There is, however, a gradual increase in C/C_0 with increasing pore volumes, suggesting some blocking or detachment of deposited PHSNs. As a first layer of deposited nanoparticles is formed, the trajectories of the subsequent nanoparticles are significantly impacted by this monolayer of deposited particles, a phenomenon previously referred to as the shadow effect [61]. The extent of the influence of the shadow effect in subsequent particle trajectory is directly related to the hydrodynamic interactions and electrostatic double layer repulsion. Therefore, as the conditions become unfavorable (lower pH and higher IS), repulsion forces decrease, thus increasing both the surface coverage of deposited nanoparticles on the sand grains and the blocking effects in the nanoparticle transport profiles.

IS Effect on the Transport Behavior. The effect of IS in the transport of SSNs and PHSNs in saturated porous media was evaluated at pH 9.5 and at the same SiO_2 concentration of 100 ppm. The BTCs for SSNs (Figure 5a) showed that the values for relative effluent concentration at 9 PVs decreased as the IS increased, from 0.99 at IS 1 mM, to 0.96 at IS 10 mM and then 0.92 at IS 100 mM, which was expected and is consistent with the literature [20, 59]. The addition of salt increases the number of counter-ions migrating to the solvation layer of the nanoparticles, thus decreasing the Debye-length and the repulsive electrostatic forces. Although the total interaction energies calculated yielded a lowered energy barrier, a weak secondary minimum (-2 k_bT) was obtained only at IS of 100 mM.

The values for relative effluent concentrations at 9 PV in the BTCs for PHSN (Figure 5b) also decreased with increasing IS, from 0.94 at IS 1 mM to 0.88 at IS 10 mM and then 0.34 at IS 100 mM. Once again, the mobility PHSNs was much more affected by the change in IS than for SSNs. The similarity in the BTC shape with changes in pH and IS suggests that similar deposition processes are involved. As for the SSNs at pH 9.5 and IS at 100 mM, a weak secondary minimum for PHSNs was calculated from the interaction energy profiles at an IS of 100 mM.

Overall, low pH and high IS decreased the mobility of the nanoparticles in porous media. We observed similar trends between SSN and PHSN: (i) As pH decreased, zeta potential also decreased, which is expected because the isoelectric point of bare SiO_2 is around pH = 2 [62-64]. (ii) As IS increased, zeta potential decreased as a result of the stabilization of the excess ions in the electrical double layer of each nanoparticle by the counter-ions from the NaCl added. In both cases, a decrease in zeta potential led to a decrease in the intensity of repulsion forces between nanoparticles and between nanoparticles and sand. However, the increased retention of PHSNs compared to the SSNs, which is non-intuitive because both particles have comparable sizes (Figure 1) and surface chemical composition (Figure 2c). The DLVO interaction energies calculated are qualitatively in agreement with the mobility trends for SSN and PHSN, but the calculated values are not consistent in several instances. For example, if we compare the particle-collector interaction resulting energy profiles for Exp. 5 (SSNs, pH 9.5, IS 100 mM, Figure 6c) with Exp. 10 (PHSNs, pH 9.5, IS 100 mM, Figure 6d) the heights of energy barriers were comparable, and yet, the steady-state relative effluent concentrations were 0.34 and 0.96 for PHSNs and SSNs, respectively. A theoretical analysis of DLVO interaction forces between SSN or PHSN and collector surfaces suggested relatively small differences in the magnitude of the interaction forces [50], and is in agreement with the calculations in this study. It is likely that the surface structure differences caused by the concave asperities in the PHSNs caused by the pores played an important role in the mobility of these particles.

Single Collector Contact Efficiencies (η_0) and Particle-Collector Attachment Efficiencies (α_{pc}). The η_0 values as a function of particle radius (a_p) for SSNs (Figure 7a) and PHSNs (Figure 7b) were calculated based on expressions derived elsewhere [51-56]. The

expressions and parameters used to estimate the η_0 can be found in Table S3 and Table S4, respectively.

The average η_0 predicted for SSNs (a_p = 92 nm) and PHSN (a_p = 103 nm) were 0.007 and 0.005, respectively. The η_0 were slightly greater for SSNs, which is contrary to observations of lower mobility of PHSNs in the column experiments. To assess the size difference effect between SSNs and PHSNs, the η_0 ratio was plotted as a function of particle size in Figure 7c. For any particle radius below 100 nm, SSNs and PHSNs have very similar predictions for η_0. For any particle radius above 100 nm, the predicted η_0 for SSNs surpassed the predicted η_0 for PHSNs, indicating more chance of retention for SSNs than for PHSNs. Therefore, η_0 could not explain why such inconsistencies with the experimental data exist.

The α_{pc} values remained below 0.04 for all experimental conditions with SSNs, whereas they reached 0.54 and 0.59 for PHSNs at pH 4.5 and IS 1 mM, and at pH 9.5 and IS 100 mM, respectively, which were the conditions where retention was more pronounced. The α_{pc} values (Table S5) were calculated with Equation (3) below.

$$\alpha_{pc} = -\frac{2}{3}\frac{d_c}{(1-n)L\eta_0}\ln\left(\frac{C}{C_0}\right) \quad (3)$$

Surface Roughness and the DLVO Theory. Deviations from DLVO predictions due to nanoscale physical heterogeneity have been previously reported [65-74]. These deviations happen because standard DLVO theory assumes that particle and collector surfaces are geometrically smooth and homogeneous, when in reality colloid may possess some degree of roughness [67]. Modeling and experimental data have demonstrated that surface roughness reduces the repulsive energy barriers, and in some cases eliminates them altogether [67-69, 72]. For instance, Liang, et al. [71] observed enhanced retention of silver nanoparticles in porous media with higher surface roughness (SR). Retention was 6.8-fold higher in relatively rough sand particles (root mean square roughness, S_q = 524 nm) when compared to the experimental condition using relatively smooth sand (S_q = 93 nm).

Specifically, two phenomena are relevant: (i) the concave asperities in PHSN surface, caused by the presence of pores in the surface, result in the separation distance among particle-

particle and/or particle-collector surfaces becoming larger at the pores, when compared to that of SSNs [69] as depicted in Figure 8. Generally, as the separation distance increases, overall repulsive electrostatic forces generally decay faster than van der Waals interactions [75], resulting in enhanced attraction to the collector surface. (ii) The roughness caused by the asperities on PHSN surface alter the flow field around the particle during the column experiments, enhancing resisting adhesive torque and diminishing applied hydrodynamic torque [76]. These effects likely led to enhanced colloid immobilization on the collector in this study.

It is also important to note that this work has assessed the transport behavior of SiO2 NPs in saturated sand, and thus, will differ from actual agricultural conditions. Agricultural soils are generally unsaturated, with some exceptions, such as when the soil is irrigated or when it rains. Agricultural soil may also contain high organic matter content and other types of contaminants that could complex with the NPs and influence their mobility. These conditions, however, are not replicated in our experimental setting. Nevertheless, the use of saturated sand served as model towards a first step in assessing the fundamental differences in the transport profile of SSNs and PHSNs and how their structure plays a role in their mobility.

Conclusions

Herein, we synthesized, characterized, and investigated the mobility of SSNs and PHSNs in a saturated sand-packed column in various pH and IS conditions. As expected, the zeta potential of both sets of particles approached lower absolute values as pH became more acidic and closer to the isoelectric point of SiO_2 nanoparticles. On the other hand, zeta potential approached lower absolute values as IS increased. The decrease in zeta potential indicates a decrease in the repulsive forces between nanoparticles, which in turn led to a small extent of agglomeration, and higher PdI.

During the column experiments, deposition was enhanced by the decrease of pH and increase of zeta potential, as such conditions deteriorate (acidic pH and high salinity) the overall colloidal stability of SiO_2 nanoparticles in suspension. The PHSNs, however, experienced a higher degree of deposition when compared to SSNs. DLVO energy profiles and single

collector contact efficiency values were unable to explain why such discrepancies existed, and surface roughness likely contributed to the different extents of deposition. The surface roughness was not factored into the DLVO calculations because of the high complexity of the calculations and the many assumptions needed. The surface roughness related concave asperities of the pores lowered the repulsive energy barriers and led to more deposition.

This study elucidates how nanoparticle architecture can influence their mobility in porous media and highlights the importance of a thorough experimental analysis of the fate and transport of nanoparticles of different architecture that are likely to be discharged in the environment, such those intended for use in nano-enabled agriculture.

Declaration of competing interest

The authors declare that they have no known competing financial interests or personal relationships that could have appeared to influence the work reported in this paper.

CRediT author statement

Vinicius Bueno: Conceptualization, Methodology, Investigation, Writing-Original Draft, Visualization. Alessandro Bosi: Conceptualization, Methodology, Investigation, Writing-Review & Editing. Tiziana Tosco: Conceptualization, Investigation, Writing Review & Editing, Funding acquisition. Subhasis Ghoshal: Conceptualization, Investigation, Writing-Review & Editing, Supervision, Funding acquisition.

Acknowledgments

The research was funded by the Natural Sciences and Engineering Research Council of Canada (grant nos. RGPIN-2016-05022, STPGP 506450-17). V.B. was supported in part by a McGill Engineering Doctoral Award. A.B. was supported in part by Politecnico di Torino for the M.Sc. thesis abroad program. The authors acknowledge the assistance of Sofia Credaro in text editing of the manuscript.

FIGURES

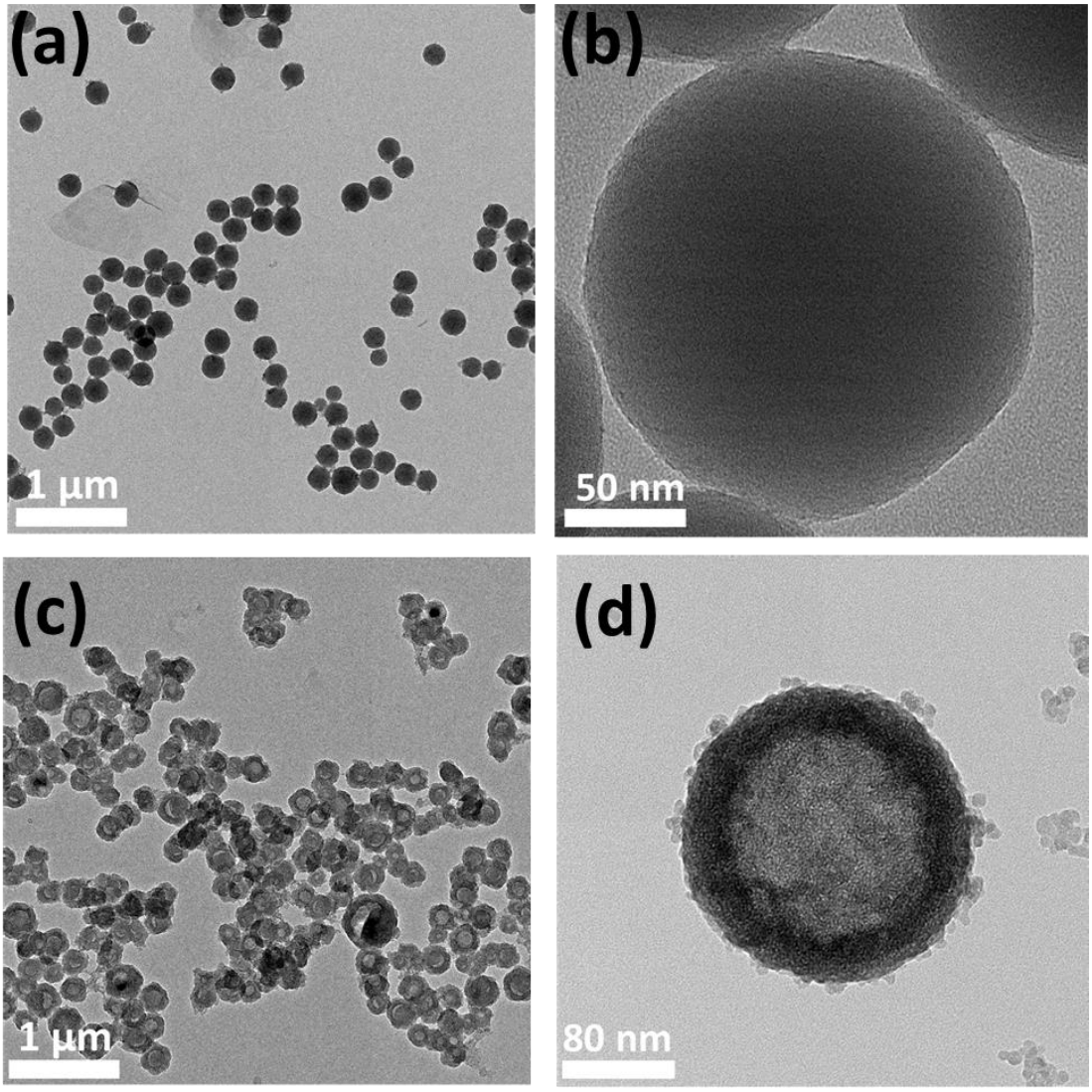

Figure 1. TEM images of (a and b) SSNs and (c and d) PHSNs. The images on the right exhibit more magnified images of singular (b) SSN and (d) PHSN to show the different features between both structures. Although both structures are spherically shaped, PHSNs feature a hollow core and pores. The latter is directly responsible for the increased surface area and roughness of PHSNs when compared to SSNs.

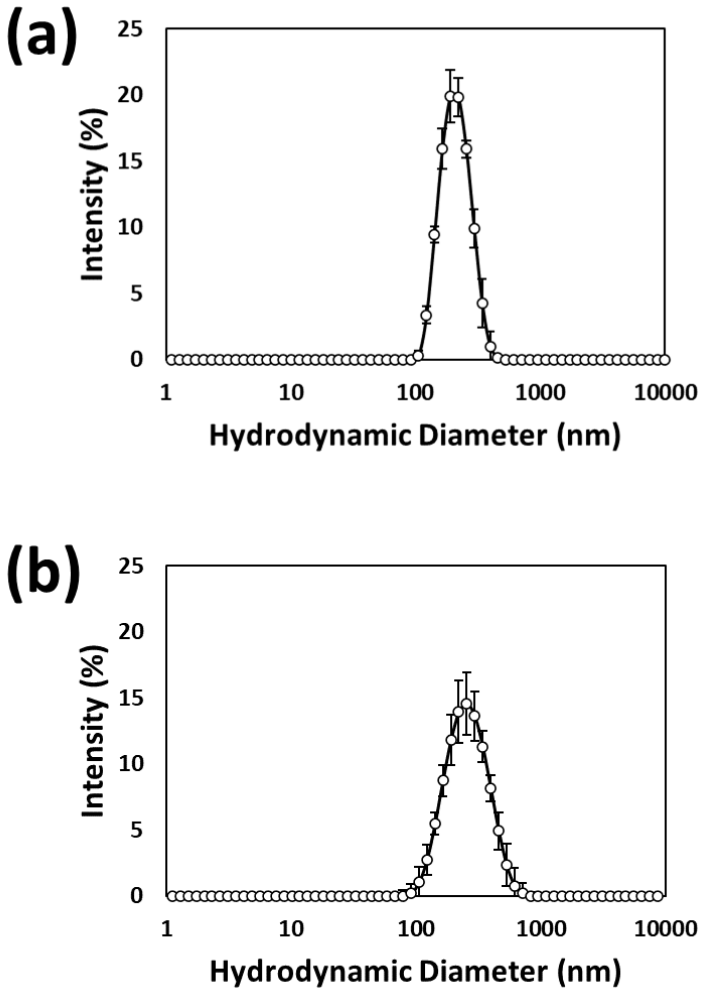

238

239 **Figure 2.** Particle size distribution at pH 9.5 and IS 1 mM of (a) SSNs and (b) PHSNs. The
240 width of the PHSN size distribution is broader than that for SSN, indicating a higher PdI as
241 confirmed in Table 1.

242

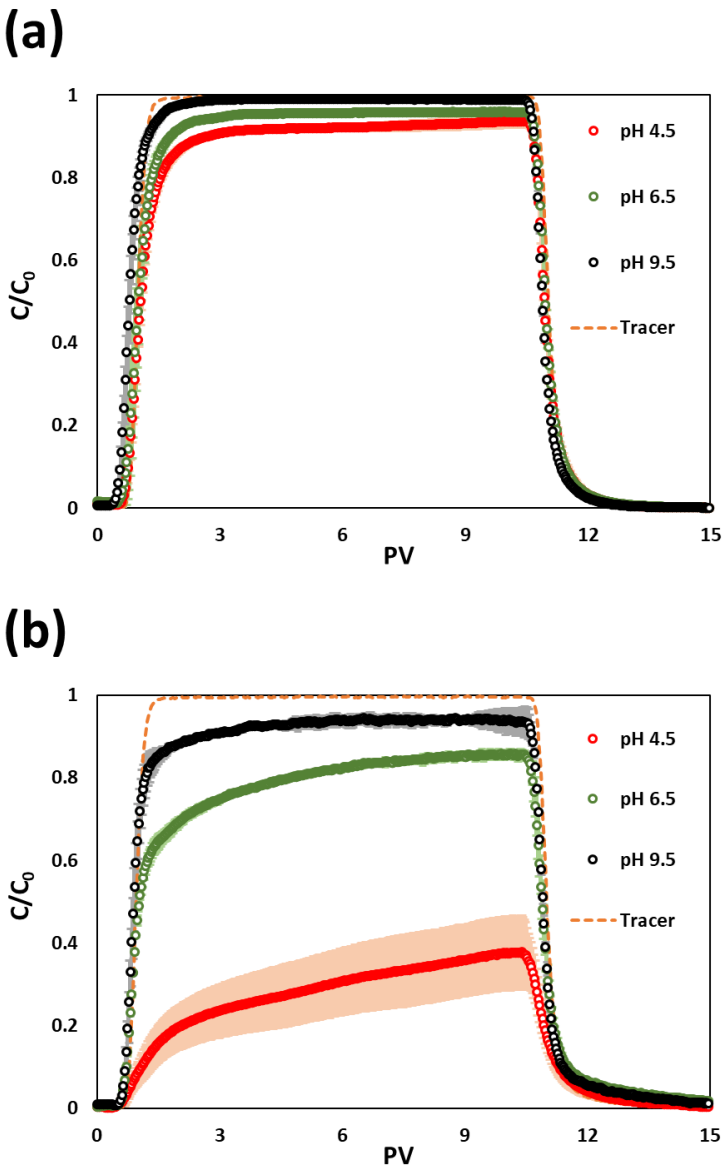

Figure 3. BTCs at fixed IS 1 mM and varying pH for (a) SSNs and (b) PHSNs. The shaded zones represent the standard deviation of the particle concentration run in triplicates. Wider shaded areas represent greater standard deviation among replicates. The conditions with no visible shaded areas represent runs with not relevant difference among replicates.

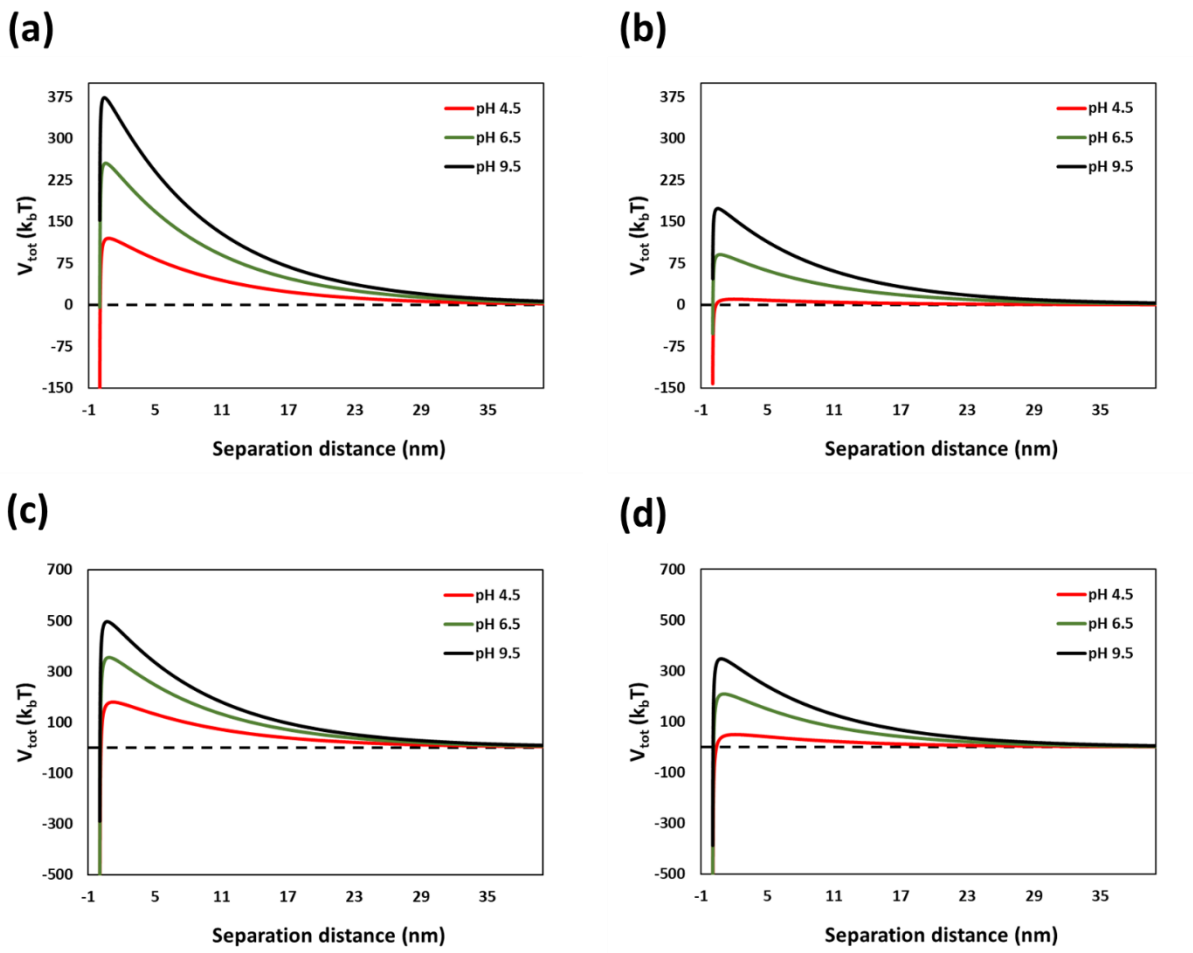

Figure 4. DLVO energy profiles at fixed IS 1 mM and varying pH for (a) SSN particle-particle interactions, (b) PHSN particle-particle interactions, (c) SSN particle-collector interactions, and (d) PHSN particle-collector interactions.

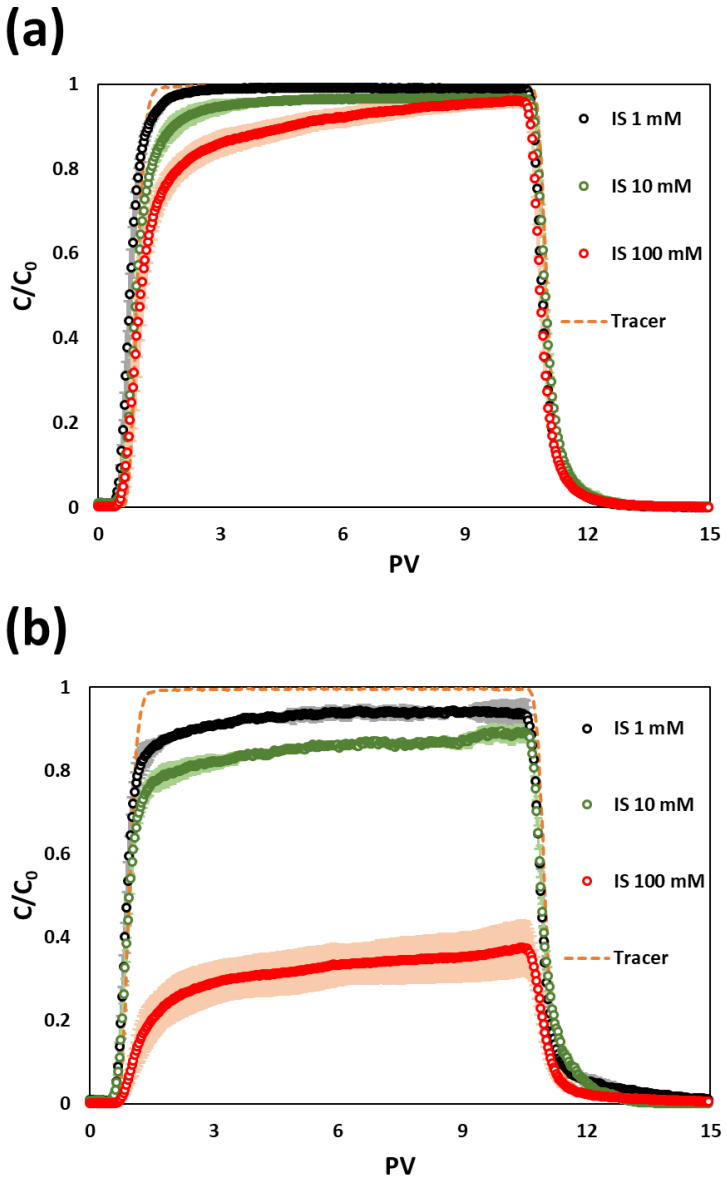

255

256 **Figure 5.** BTCs at fixed pH 9.5 and varying IS for (a) SSNs and (b) PHSNs. The shaded
257 zones represent the standard deviation of the particle concentration run in triplicates. Wider
258 shaded areas represent greater standard deviation among replicates. The conditions with no
259 visible shaded areas represent runs with not relevant difference among replicates.

260

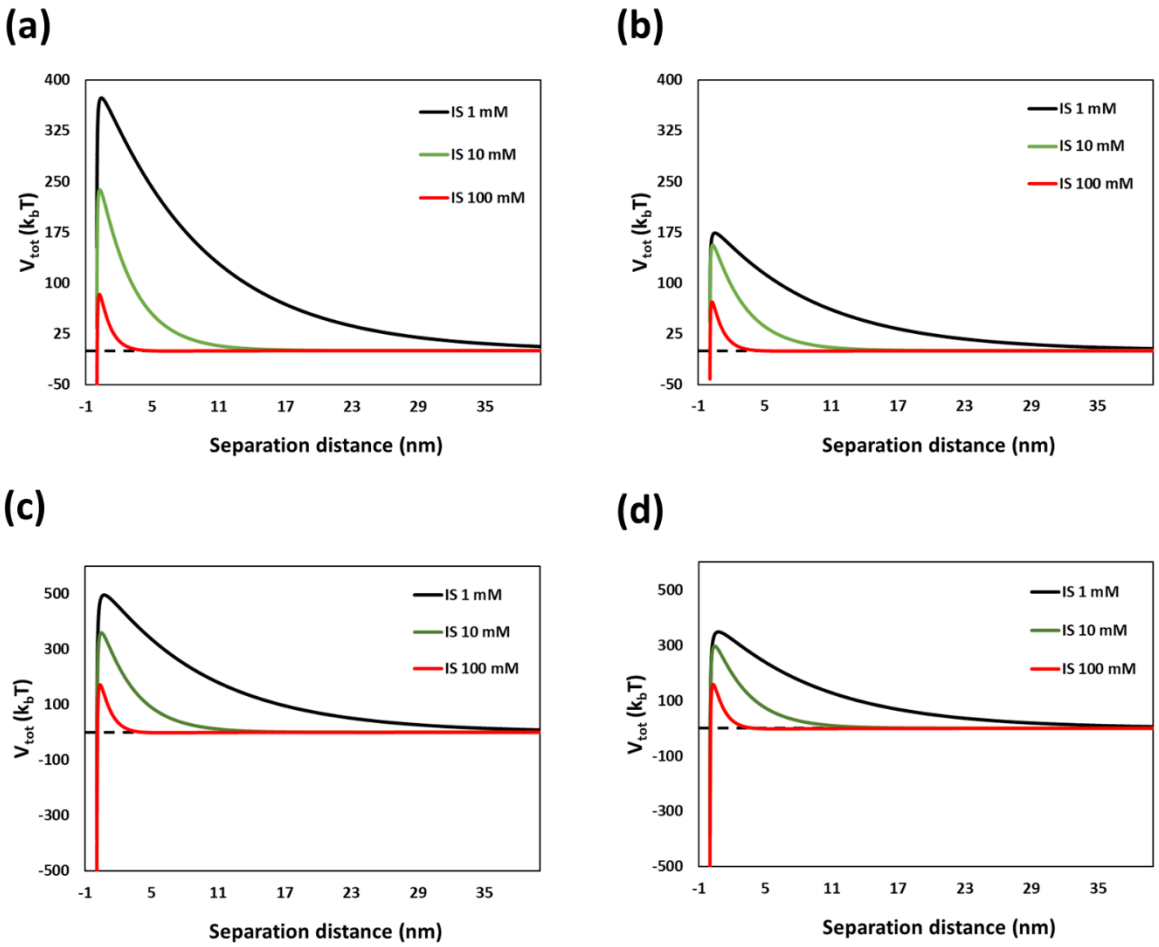

Figure 6. DLVO energy profiles at fixed pH 9.5 and varying IS for (a) SSN particle-particle interactions, (b) PHSN particle-particle interactions, (c) SSN particle-collector interactions, and (d) PHSN particle-collector interactions.

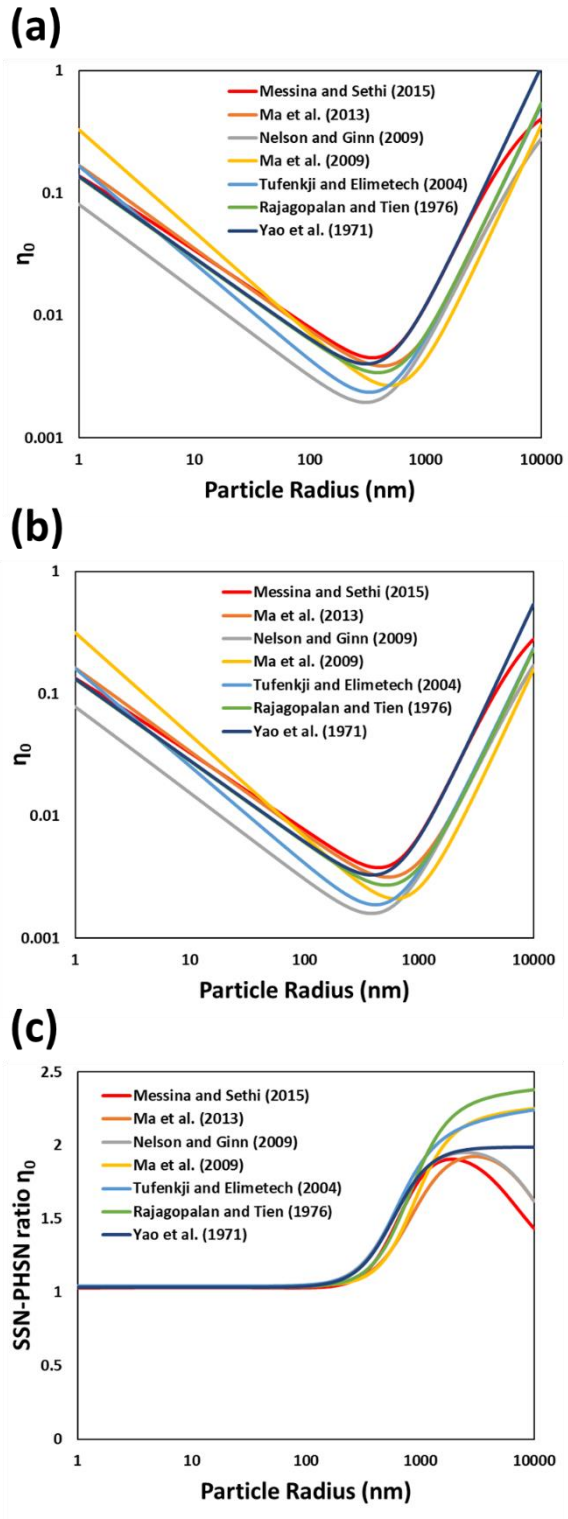

Figure 7. Estimates of η_0 for (a) SSNs and (b) PHSNs, and (c) the SSN-PHSN η_0 ratio.

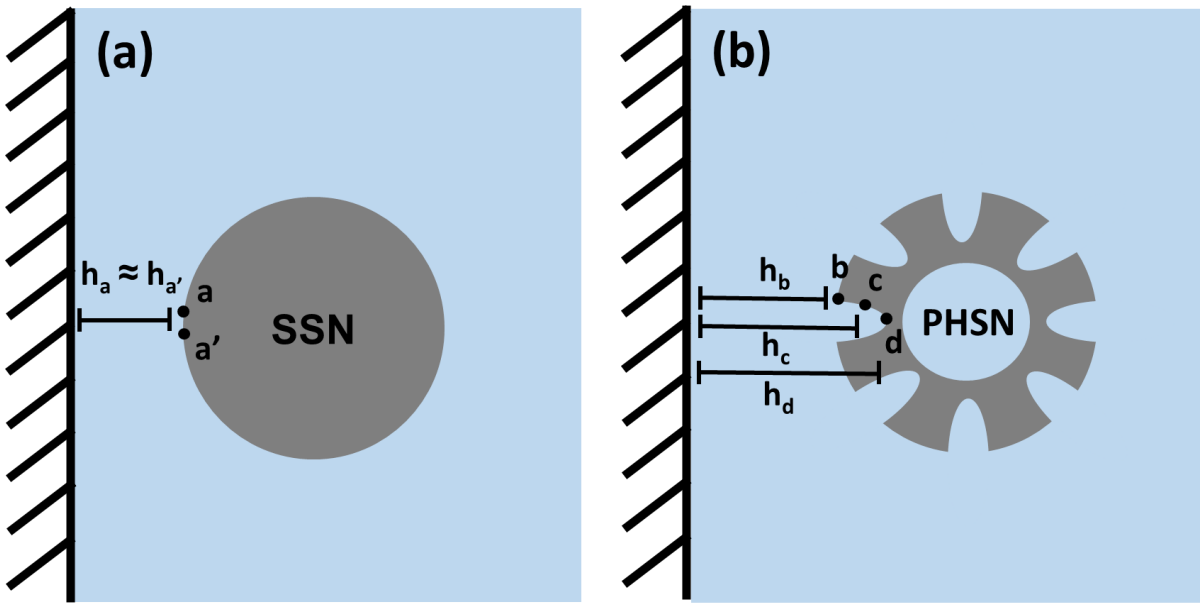

Figure 8. Schematic representation of the distance between sites in the SSN (a) and PHSN (b), and a hypothetical surface. For SSNs, the distance from point *a* to the surface, h_a, and the distance from a relatively distant point *a'* to the same surface, $h_{a'}$, are approximately the same. Meanwhile, in PHSNs, the distances h_b, h_c and h_d may vary significantly, even if they are at the same distance as points *a* and *a'* in scheme (a). Effectively, the overall separation distance between rough spherical surfaces and a hypothetical surface is larger than the distance between smooth spherical surfaces and a hypothetical surface.

REFERENCES

[1] T. Hofmann, G.V. Lowry, S. Ghoshal, N. Tufenkji, D. Brambilla, J.R. Dutcher, L.M. Gilbertson, J.P. Giraldo, J.M. Kinsella, M.P. Landry, Technology readiness and overcoming barriers to sustainably implement nanotechnology-enabled plant agriculture, Nature Food 1(7) (2020) 416-425.

[2] M. Kah, N. Tufenkji, J.C. White, Nano-enabled strategies to enhance crop nutrition and protection, Nature nanotechnology 14(6) (2019) 532-540.

[3] G.V. Lowry, A. Avellan, L.M. Gilbertson, Opportunities and challenges for nanotechnology in the agri-tech revolution, Nature nanotechnology 14(6) (2019) 517-522.

[4] A. Ditta, How helpful is nanotechnology in agriculture?, Advances in Natural Sciences: Nanoscience and Nanotechnology 3(3) (2012) 033002.

[5] P.M. Kopittke, E. Lombi, P. Wang, J.K. Schjoerring, S. Husted, Nanomaterials as fertilizers for improving plant mineral nutrition and environmental outcomes, Environmental Science: Nano 6(12) (2019) 3513-3524.

[6] M.C. Camara, E.V.R. Campos, R.A. Monteiro, A.d.E. Santo Pereira, P.L. de Freitas Proença, L.F. Fraceto, Development of stimuli-responsive nano-based pesticides: emerging opportunities for agriculture, Journal of nanobiotechnology 17(1) (2019) 1-19.

[7] J.L. de Oliveira, E.V.R. Campos, M. Bakshi, P. Abhilash, L.F. Fraceto, Application of nanotechnology for the encapsulation of botanical insecticides for sustainable agriculture: prospects and promises, Biotechnology advances 32(8) (2014) 1550-1561.

[8] R. Grillo, P.C. Abhilash, L.F. Fraceto, Nanotechnology applied to bio-encapsulation of pesticides, Journal of Nanoscience and Nanotechnology 16(1) (2016) 1231-1234.

[9] E. Epstein, The anomaly of silicon in plant biology, Proceedings of the National Academy of Sciences 91(1) (1994) 11-17.

[10] M. Luyckx, J.-F. Hausman, S. Lutts, G. Guerriero, Silicon and plants: current knowledge and technological perspectives, Frontiers in Plant Science 8 (2017) 411.

[11] M. El-Shetehy, A. Moradi, M. Maceroni, D. Reinhardt, A. Petri-Fink, B. Rothen-Rutishauser, F. Mauch, F. Schwab, Silica nanoparticles enhance disease resistance in Arabidopsis plants, Nature Nanotechnology (2020) 1-10.

[12] M.E. Abdel-Haliem, H.S. Hegazy, N.S. Hassan, D.M. Naguib, Effect of silica ions and nano silica on rice plants under salinity stress, Ecological Engineering 99 (2017) 282-289.

[13] E.A. Attia, N. Elhawat, Combined foliar and soil application of silica nanoparticles enhances the growth, flowering period and flower characteristics of marigold (Tagetes erecta L.), Scientia Horticulturae 282 (2021) 110015.

[14] P. Zhao, W. Yuan, C. Xu, F. Li, L. Cao, Q. Huang, Enhancement of spirotetramat transfer in cucumber plant using mesoporous silica nanoparticles as carriers, Journal of agricultural and food chemistry 66(44) (2018) 11592-11600.

[15] J. Cui, Y. Li, Q. Jin, F. Li, Silica nanoparticles inhibit arsenic uptake into rice suspension cells via improving pectin synthesis and the mechanical force of the cell wall, Environmental Science: Nano 7(1) (2020) 162-171.
[16] L. Tian, J. Shen, G. Sun, B. Wang, R. Ji, L. Zhao, Foliar Application of SiO2 Nanoparticles Alters Soil Metabolite Profiles and Microbial Community Composition in the Pakchoi (Brassica chinensis L.) Rhizosphere Grown in Contaminated Mine Soil, Environmental Science & Technology 54(20) (2020) 13137-13146.
[17] H. Fatemi, B.E. Pour, M. Rizwan, Foliar application of silicon nanoparticles affected the growth, vitamin C, flavonoid, and antioxidant enzyme activities of coriander (Coriandrum sativum L.) plants grown in lead (Pb)-spiked soil, Environmental Science and Pollution Research 28(2) (2021) 1417-1425.
[18] I. Kim, A. Taghavy, D. DiCarlo, C. Huh, Aggregation of silica nanoparticles and its impact on particle mobility under high-salinity conditions, Journal of Petroleum Science and Engineering 133 (2015) 376-383.
[19] S. Al-Anssari, L. Nwidee, M. Ali, J.S. Sangwai, S. Wang, A. Barifcani, S. Iglauer, Retention of silica nanoparticles in limestone porous media, SPE/IATMI Asia Pacific Oil & Gas Conference and Exhibition, Society of Petroleum Engineers, 2017.
[20] C. Wang, A.D. Bobba, R. Attinti, C. Shen, V. Lazouskaya, L.-P. Wang, Y. Jin, Retention and transport of silica nanoparticles in saturated porous media: effect of concentration and particle size, Environ. Sci. Technol. 46(13) (2012) 7151-7158.
[21] Y. Qin, Z. Wen, W. Zhang, J. Chai, D. Liu, S. Wu, Different roles of silica nanoparticles played in virus transport in saturated and unsaturated porous media, Environmental Pollution 259 (2020) 113861.
[22] M. Zhang, D. Li, Z. Ye, S. Wang, N. Xu, F. Wang, S. Liu, J. Chen, H. Gu, Effect of humic acid on the sedimentation and transport of nanoparticles silica in water-saturated porous media, Journal of Soils and Sediments 20(2) (2020) 911-920.
[23] L. HonetschlÄgerová, P. Janouškovcová, M. Kubal, Enhanced transport of Si-coated nanoscale zero-valent iron particles in porous media, Environ. Technol. 37(12) (2016) 1530-1538.
[24] J. Li, S. Bhattacharjee, S. Ghoshal, The effects of viscosity of carboxymethyl cellulose on aggregation and transport of nanoscale zerovalent iron, Colloids and Surfaces A: Physicochemical and Engineering Aspects 481 (2015) 451-459.
[25] J. Chen, Q. Ji, P. Zheng, T. Chen, C. Wang, Q. Mahmood, Floatation and control of granular sludge in a high-rate anammox reactor, water research 44(11) (2010) 3321-3328.
[26] S. Ishii, J. Bell, F. Marshall, Phytotoxic risk assessment of ambient air pollution on agricultural crops in Selangor State, Malaysia, Environmental Pollution 150(2) (2007) 267-279.
[27] F. Torney, B.G. Trewyn, V.S.-Y. Lin, K. Wang, Mesoporous silica nanoparticles deliver DNA and chemicals into plants, Nature nanotechnology 2(5) (2007) 295-300.
[28] T.M. Abdelrahman, X. Qin, D. Li, I.A. Senosy, M. Mmby, H. Wan, J. Li, S. He, Pectinase-responsive carriers based on mesoporous silica nanoparticles for improving the translocation and fungicidal activity of prochloraz in rice plants, Chemical Engineering Journal 404 (2021) 126440.

[29] O. Plohl, S. Gyergyek, L.F. Zemljič, Mesoporous silica nanoparticles modified with N-rich polymer as a potentially environmentally-friendly delivery system for pesticides, Microporous and Mesoporous Materials 310 (2021) 110663.
[30] Y. Xu, C. Xu, Q. Huang, L. Cao, F. Teng, P. Zhao, M. Jia, Size Effect of Mesoporous Silica Nanoparticles on Pesticide Loading, Release, and Delivery in Cucumber Plants, Applied Sciences 11(2) (2021) 575.
[31] X. Gao, A. Kundu, V. Bueno, A.A. Rahim, S. Ghoshal, Uptake and Translocation of Mesoporous SiO2-Coated ZnO Nanoparticles to Solanum lycopersicum Following Foliar Application, Environmental Science & Technology (2021).
[32] J. Feng, W. Chen, Y. Shen, Q. Chen, J. Yang, M. Zhang, W. Yang, S. Yuan, Fabrication of abamectin-loaded mesoporous silica nanoparticles by emulsion-solvent evaporation to improve photolysis stability and extend insecticidal activity, Nanotechnology 31(34) (2020) 345705.
[33] F. Liu, L.-X. Wen, Z.-Z. Li, W. Yu, H.-Y. Sun, J.-F. Chen, Porous hollow silica nanoparticles as controlled delivery system for water-soluble pesticide, Materials research bulletin 41(12) (2006) 2268-2275.
[34] Z.-Z. Li, S.-A. Xu, L.-X. Wen, F. Liu, A.-Q. Liu, Q. Wang, H.-Y. Sun, W. Yu, J.-F. Chen, Controlled release of avermectin from porous hollow silica nanoparticles: Influence of shell thickness on loading efficiency, UV-shielding property and release, Journal of Controlled Release 111(1-2) (2006) 81-88.
[35] L.X. Wen, Z.Z. Li, H.K. Zou, A.Q. Liu, J.F. Chen, Controlled release of avermectin from porous hollow silica nanoparticles, Pest Management Science: formerly Pesticide Science 61(6) (2005) 583-590.
[36] V. Bueno, S. Ghoshal, Self-Assembled Surfactant-Templated Synthesis of Porous Hollow Silica Nanoparticles: Mechanism of Formation and Feasibility of Post-Synthesis Nanoencapsulation, Langmuir 36(48) (2020) 14633-14643.
[37] S. Torkzaban, J. Wan, T.K. Tokunaga, S.A. Bradford, Impacts of bridging complexation on the transport of surface-modified nanoparticles in saturated sand, Journal of contaminant hydrology 136 (2012) 86-95.
[38] T. Raychoudhury, N. Tufenkji, S. Ghoshal, Aggregation and deposition kinetics of carboxymethyl cellulose-modified zero-valent iron nanoparticles in porous media, Water research 46(6) (2012) 1735-1744.
[39] T. Raychoudhury, N. Tufenkji, S. Ghoshal, Straining of polyelectrolyte-stabilized nanoscale zero valent iron particles during transport through granular porous media, Water research 50 (2014) 80-89.
[40] T. Tosco, J. Bosch, R.U. Meckenstock, R. Sethi, Transport of ferrihydrite nanoparticles in saturated porous media: role of ionic strength and flow rate, Environmental science & technology 46(7) (2012) 4008-4015.
[41] W. Stöber, A. Fink, E. Bohn, Controlled growth of monodisperse silica spheres in the micron size range, Journal of colloid and interface science 26(1) (1968) 62-69.
[42] I. Oliviera, A. Demond, A. Salehzadeh, Packing of sands for the production of homogeneous porous media, Soil Science Society of America Journal 60(1) (1996) 49-53.
[43] R.J. Hunter, Zeta potential in colloid science: principles and applications, Academic press2013.

[44] J. Gregory, Approximate expressions for retarded van der Waals interaction, Journal of colloid and interface science 83(1) (1981) 138-145.
[45] J. De Vicente, A. Delgado, R. Plaza, J. Durán, F. González-Caballero, Stability of cobalt ferrite colloidal particles. Effect of pH and applied magnetic fields, Langmuir 16(21) (2000) 7954-7961.
[46] E. Ruckenstein, D.C. Prieve, Adsorption and desorption of particles and their chromatographic separation, AIChE Journal 22(2) (1976) 276-283.
[47] T. Phenrat, Y. Liu, R.D. Tilton, G.V. Lowry, Adsorbed polyelectrolyte coatings decrease Fe0 nanoparticle reactivity with TCE in water: conceptual model and mechanisms, Environmental science & technology 43(5) (2009) 1507-1514.
[48] D.M. Lipkin, J.N. Israelachvili, D.R. Clarke, Estimating the metal-ceramic van der Waals adhesion energy, Philosophical Magazine A 76(4) (1997) 715-728.
[49] C. Shen, S.A. Bradford, M. Flury, Y. Huang, Z. Wang, B. Li, DLVO interaction energies for hollow particles: The filling matters, Langmuir 34(43) (2018) 12764-12775.
[50] C. Shen, S. Bradford, Z. Wang, Y. Huang, Y. Zhang, B. Li, DLVO interaction energies between hollow spherical particles and collector surfaces, Langmuir 33(40) (2017) 10455-10467.
[51] K.-M. Yao, M.T. Habibian, C.R. O'Melia, Water and waste water filtration. Concepts and applications, Environ. Sci. Technol. 5(11) (1971) 1105-1112.
[52] R. Rajagopalan, C. Tien, Trajectory analysis of deep-bed filtration with the sphere-in-cell porous media model, AIChE J. 22(3) (1976) 523-533.
[53] N. Tufenkji, M. Elimelech, Correlation equation for predicting single-collector efficiency in physicochemical filtration in saturated porous media, Environ. Sci. Technol. 38(2) (2004) 529-536.
[54] H. Ma, J. Pedel, P. Fife, W.P. Johnson, Hemispheres-in-cell geometry to predict colloid deposition in porous media, Environ. Sci. Technol. 43(22) (2009) 8573-8579.
[55] K.E. Nelson, T.R. Ginn, New collector efficiency equation for colloid filtration in both natural and engineered flow conditions, Water Resources Research 47(5) (2011).
[56] H. Ma, M. Hradisky, W.P. Johnson, Extending applicability of correlation equations to predict colloidal retention in porous media at low fluid velocity, Environ. Sci. Technol. 47(5) (2013) 2272-2278.
[57] F. Messina, D.L. Marchisio, R. Sethi, An extended and total flux normalized correlation equation for predicting single-collector efficiency, Journal of colloid and interface science 446 (2015) 185-193.
[58] K. Suttiponparnit, J. Jiang, M. Sahu, S. Suvachittanont, T. Charinpanitkul, P. Biswas, Role of surface area, primary particle size, and crystal phase on titanium dioxide nanoparticle dispersion properties, Nanoscale Res Lett 6(1) (2011) 27.
[59] Q. Liu, Z. Sun, J.C. Santamarina, Transport and adsorption of silica nanoparticles in carbonate reservoirs: A sand column study, Energy Fuels 33(5) (2019) 4009-4016.
[60] S. Xu, B. Gao, J.E. Saiers, Straining of colloidal particles in saturated porous media, Water Resources Research 42(12) (2006).

[61] C.-H. Ko, M. Elimelech, The “shadow effect” in colloid transport and deposition dynamics in granular porous media: measurements and mechanisms, Environmental science & technology 34(17) (2000) 3681-3689.
[62] A. Lazaro, N. Vilanova, L.D. Barreto Torres, G. Resoort, I.K. Voets, H. Brouwers, Synthesis, polymerization, and assembly of nanosilica particles below the isoelectric point, Langmuir 33(51) (2017) 14618-14626.
[63] K.R. Iler, The chemistry of silica, Solubility, polymerization, colloid and surface properties and biochemistry of silica (1979).
[64] H.E. Bergna, W.O. Roberts, Colloidal silica: fundamentals and applications, CRC Press2005.
[65] Y.I. Rabinovich, J.J. Adler, A. Ata, R.K. Singh, B.M. Moudgil, Adhesion between nanoscale rough surfaces: I. Role of asperity geometry, Journal of colloid and interface science 232(1) (2000) 10-16.
[66] J. Katainen, M. Paajanen, E. Ahtola, V. Pore, J. Lahtinen, Adhesion as an interplay between particle size and surface roughness, Journal of Colloid and Interface Science 304(2) (2006) 524-529.
[67] L. Suresh, J.Y. Walz, Effect of surface roughness on the interaction energy between a colloidal sphere and a flat plate, Journal of Colloid and Interface Science 183(1) (1996) 199-213.
[68] E.M. Hoek, S. Bhattacharjee, M. Elimelech, Effect of membrane surface roughness on colloid− membrane DLVO interactions, Langmuir 19(11) (2003) 4836-4847.
[69] E.M. Hoek, G.K. Agarwal, Extended DLVO interactions between spherical particles and rough surfaces, Journal of Colloid and Interface science 298(1) (2006) 50-58.
[70] C. Shen, Y. Jin, J. Zhuang, T. Li, B. Xing, Role and importance of surface heterogeneities in transport of particles in saturated porous media, Critical Reviews in Environmental Science and Technology 50(3) (2020) 244-329.
[71] Y. Liang, J. Zhou, Y. Dong, E. Klumpp, J. Šimůnek, S.A. Bradford, Evidence for the critical role of nanoscale surface roughness on the retention and release of silver nanoparticles in porous media, Environmental Pollution 258 (2020) 113803.
[72] S. Bhattacharjee, C.-H. Ko, M. Elimelech, DLVO interaction between rough surfaces, Langmuir 14(12) (1998) 3365-3375.
[73] S.A. Bradford, S. Torkzaban, Colloid interaction energies for physically and chemically heterogeneous porous media, Langmuir 29(11) (2013) 3668-3676.
[74] C. Jin, W. Zhao, S.D. Normani, P. Zhao, M.B. Emelko, Synergies of media surface roughness and ionic strength on particle deposition during filtration, Water research 114 (2017) 286-295.
[75] M.W. Hahn, C.R. O'Melia, Deposition and reentrainment of Brownian particles in porous media under unfavorable chemical conditions: Some concepts and applications, Environmental science & technology 38(1) (2004) 210-220.
[76] S.A. Bradford, S. Torkzaban, A. Shapiro, A theoretical analysis of colloid attachment and straining in chemically heterogeneous porous media, Langmuir 29(23) (2013) 6944-6952.